

## **The Influence of Testing Conditions on State of Health Estimations of Electric Vehicle Lithium-Ion Batteries Using an Incremental Capacity Analysis**

Gismero, Alejandro; Dubarry, Matthieu; Guo, Jia; Stroe, Daniel-Ioan; Scholtz, Erik

*Published in:*  
Batteries

*DOI (link to publication from Publisher):*  
[10.3390/batteries9120568](https://doi.org/10.3390/batteries9120568)

*Creative Commons License*  
CC BY 4.0

*Publication date:*  
2023

*Document Version*  
Publisher's PDF, also known as Version of record

[Link to publication from Aalborg University](#)

*Citation for published version (APA):*

Gismero, A., Dubarry, M., Guo, J., Stroe, D.-I., & Scholtz, E. (2023). The Influence of Testing Conditions on State of Health Estimations of Electric Vehicle Lithium-Ion Batteries Using an Incremental Capacity Analysis. *Batteries*, 9(12), Article 568. <https://doi.org/10.3390/batteries9120568>

### **General rights**

Copyright and moral rights for the publications made accessible in the public portal are retained by the authors and/or other copyright owners and it is a condition of accessing publications that users recognise and abide by the legal requirements associated with these rights.

- Users may download and print one copy of any publication from the public portal for the purpose of private study or research.
- You may not further distribute the material or use it for any profit-making activity or commercial gain
- You may freely distribute the URL identifying the publication in the public portal -

### **Take down policy**

If you believe that this document breaches copyright please contact us at [vbn@aub.aau.dk](mailto:vbn@aub.aau.dk) providing details, and we will remove access to the work immediately and investigate your claim.



## Article

# The Influence of Testing Conditions on State of Health Estimations of Electric Vehicle Lithium-Ion Batteries Using an Incremental Capacity Analysis

Alejandro Gismero <sup>1,\*</sup> , Matthieu Dubarry <sup>2,\*</sup> , Jia Guo <sup>1</sup> , Daniel-Ioan Stroe <sup>1</sup>  and Erik Scholtz <sup>1</sup> 

<sup>1</sup> Department of Energy, Aalborg University, Pontoppidanstraede 111, 9220 Aalborg, Denmark; jgu@energy.aau.dk (J.G.); dis@energy.aau.dk (D.-I.S.); esc@energy.aau.dk (E.S.)

<sup>2</sup> Hawaii Natural Energy Institute, University of Hawaii at Manoa, 1680 East-West Road, POST 109, Honolulu, HI 96822, USA

\* Correspondence: alejandro.gismero@gmail.com (A.G.); matthieu@hawaii.edu (M.D.)

**Abstract:** The increasing growth of the second-hand electric vehicle market demands reliable methods for evaluating the state of health of deployed electric vehicle batteries. Among these methods, incremental capacity analysis is a commonly used technique for state of health evaluation via the quantification of degradation modes. While the optimal conditions for its application typically involve low currents and a controlled temperature, this cannot be easily applied to deployed batteries. It is therefore essential to understand the impact of varying charging rates and temperatures on the accuracy of the analysis. In this study, the characteristics and behavior of incremental capacity features for seven electric vehicle batteries tested under different calendar aging conditions were investigated. The results show that accurate state of health estimations under different test conditions could be obtained using specific electrochemical features.

**Keywords:** electric vehicle (EV); battery state estimation; incremental capacity analysis (ICA); lithium-ion batteries; state of health (SOH)



**Citation:** Gismero, A.; Dubarry, M.; Guo, J.; Stroe, D.-I.; Scholtz, E. The Influence of Testing Conditions on State of Health Estimations of Electric Vehicle Lithium-Ion Batteries Using an Incremental Capacity Analysis. *Batteries* **2023**, *9*, 568. <https://doi.org/10.3390/batteries9120568>

Academic Editor: Pascal Venet

Received: 23 July 2023

Revised: 23 October 2023

Accepted: 15 November 2023

Published: 25 November 2023



**Copyright:** © 2023 by the authors. Licensee MDPI, Basel, Switzerland. This article is an open access article distributed under the terms and conditions of the Creative Commons Attribution (CC BY) license (<https://creativecommons.org/licenses/by/4.0/>).

## 1. Introduction

Durability and reliability are crucial to accelerate the deployment of batteries for applications such as electric mobility and energy storage systems. Assessing them necessitates the development of effective and reliable methods to diagnose and predict battery performance. Durability is generally established from the capacity reduction caused by battery degradation and, in the case of electric vehicles (EVs), how their available range reduces with time. It is usually characterized by the battery state of health (SOH), which is associated with the ability of the battery to supply power and energy. Since capacity is usually the limiting factor in these systems, it is commonly used to define the SOH and a battery is usually considered at end of life (EOL) when the capacity drops under 80% of its initial value [1].

Accurate SOH estimation is still a challenging task because battery degradation is path-dependent [2–4]. The most direct way is to measure capacity through a full charge or discharge cycle and compare it to its initial value. However, this is impractical in deployed systems because it requires maintenance downtime which is time- and resource-demanding. Besides capacity, another parameter that is commonly used is the internal resistance, which allows tracking of the power capability of the battery. It can be measured through different methods such as pulse testing [5,6] or electrochemical impedance spectroscopy (EIS). Recently, a third approach emerged with the analysis of the voltage response of the cells. Most notably, the derivatives of the voltage, incremental capacity and differential voltage analyses (ICA and DVA, respectively), have attracted a lot of interest as these techniques allow us to not only assess the battery performance but also to quantify the degradation

modes that are taking place and thus to provide some insights into the electrochemical processes within the battery [7–10]. This work aims to improve the SOH estimation accuracy under uncontrolled conditions and outside the laboratory, with a specific focus on its application to electric vehicles. One of the key distinctions between this paper and the existing literature is the recognition of the fundamental role of peak indexing in obtaining a valid SOH estimator. This paper shows the counter-intuitive behavior of a specific parameter, referred to as P3, and demonstrates that an incomplete analysis, without a deep understanding of the underlying reactions, can lead to a misinterpretation of the incremental capacity (IC) curve. Different works have demonstrated the potential of tracking one or several indicators, also called features of interest (FOIs), of the IC curve and obtaining low SOH estimation errors [7,11–14]. An ICA is usually undertaken using low-rate charge or discharge curves which is very time consuming. This could prove problematic for deployed applications where it is necessary not only to obtain accurate results but also to obtain them in a time-effective manner. Although the testing time can be reduced by increasing the current, higher charging rates alter the IC curve shape, which drastically affects the accuracy of an ICA [15,16]. When applying this method to deployed systems, temperature is also an important factor, since it will affect the voltage response of the cells and thus might affect the accuracy of FOI determination [12,17,18].

This paper investigates the impact of different temperatures and charging rates on the voltage response of a battery designed for EVs with the goal of improving the accuracy of the SOH estimation. The comparative evaluation of various FOIs can provide more accurate and reliable information on the battery's condition under different working conditions. By studying the influence of temperature and charging rates on IC curves, this research highlights the importance of these parameters in the diagnosability of SOH in electric vehicle batteries, thereby extending the applicability of the ICA method to a wider range of conditions and enabling its extension to real-world scenarios. Section 2 describes the battery and equipment used in this work as well as the test and procedures. Section 3.1 presents the characterization of the full cell and electrodes at beginning of life (BOL), illustrating the effect of different test conditions on the IC curves. Section 3.2 applies the findings and knowledge of the previous section to determine the most suitable FOIs to evaluate SOH based on testing conditions. Finally, Section 4 summarizes the conclusions of this work. Although ICAs can be used to quantify the different mix of degradation modes associated with different usages, this is out of the scope of this paper and will be addressed in future work.

## 2. Materials and Methods

### 2.1. Battery Used

The cells used in this work were harvested from a second-generation 2018 40 kWh Nissan Leaf. The Leaf battery pack is composed of 24 modules made up of 8 pouch cells in a  $2 \times (2s2p)$  configuration [19]. Single cells from one module were carefully removed and separated for individual testing. Each cell has a capacity of 57.5 Ah and is composed of a graphite negative electrode (NE) and a  $\text{LiNi}_{0.5}\text{Mn}_{0.3}\text{Co}_{0.2}\text{O}_2$  (NMC532)-based positive electrode (PE).

### 2.2. Calendar Aging Test

The performance of a Li-ion battery undergoes progressive degradation from the time it is manufactured to the end of its useful life, and this degradation rate depends on the operating and storage conditions during that period. Since most vehicles spend a large part of their life parked, calendar aging has a significant impact on EV cell degradation and it was selected as the main focus of this work. The two main parameters that affect the life of a battery at rest are temperature and state of charge (SOC) [20]. To analyze different aging conditions, seven cells were tested under different temperature and SOC conditions for 13 months. A summary of the testing conditions is provided in Table 1.

**Table 1.** Test matrix for calendar aging.

Cell ID	Test Conditions	
	T (°C)	SOC (%)
Cal-01	5	90
Cal-02	25	90
Cal-03	35	10
Cal-04	35	50
Cal-05	35	90
Cal-06	45	90
Cal-07	45	50

To analyze how different conditions of temperature and charging current affect the IC curves, a series of tests were carried out at six different temperatures between 10 °C and 35 °C and four different C-rates between C/25 (2.3 A) and 0.87C (50 A and tester limit). For the main experiment, three cells were exposed to the same temperature (35 °C) with varying SOC levels (10%, 50%, and 90%) to evaluate the effect of the SOC. Additionally, another four cells were subjected to the same SOC conditions but different temperatures (5 °C, 25 °C, 35 °C, and 45 °C) to study the impact of temperature. After each month (30 days) of storage, a Reference Performance Test (RPT) comprising various charging rates (C/5, C/2, and 0.87C) with a constant 0.87C discharge was performed at three different temperatures (10 °C, 25 °C, and 35 °C) to measure the capacity, open circuit voltage (OCV), internal resistance, and discharging efficiency of the cells. More details about the RPT can be found in [5,21]. The RPT and aging tests were performed in a temperature-controlled environment using Memmert climate chambers (ICH 256 and UF 450 models; Memmert GmbH, Schwabach, Germany). Testing and data acquisition were performed using a DIGATRON tester (MCT-ME-50-06-24 model; Digatron Power Electronics, Aachen, Germany) with BTS-600 data acquisition software.

In addition to the full-cell testing, one of the pristine cells was disassembled to characterize the electrodes separately. The cell was opened in an argon-filled glovebox and 14 mm discs were punched from the extracted electrode sheets. The discs were washed with dimethyl carbonate and dried in an oven for 24 h to remove residual electrolyte and solvent. Coin cells were then assembled using the obtained electrode materials (NMC and graphite) as the PE and metallic lithium as the NE. A 25 µm-thick micro-porous polypropylene membrane was used as a separator and a nickel foam disc was used as the current collector on the PE side. The electrolyte was composed of 1M lithium hexafluorophosphate dissolved in a mixture of ethylene carbonate and diethyl carbonate. The test to evaluate the half cells consisted of two steps: a conditioning cycle at C/10, followed by two low rate cycles to evaluate the electrodes. These cycles were performed at C/25, between 2.65 V and 4.2 V for (NMC/Li) and between 1.5 V and 0.001 V for (graphite/Li).

All the mechanistic model simulations in this work were undertaken using the 'alawa toolbox [22,23].

### 3. Results

#### 3.1. Cell Characterization

##### 3.1.1. Full Cell Characterization

Figure 1 presents the IC curve evolution with the six temperatures for the four different charging currents at the BOL. For this graphite//NMC cells at the BOL, three IC peaks and two well-defined valleys are visible at low rates. The first peak (P1) is located at 3.50 V, the second and main one (P2) at 3.60 V, and the third and last peak (P3) at 3.85 V. The main valleys are located at 3.55 V (V1) and 3.8 V (V2). The obtained curves are in agreement with those reported in the literature for similar configurations [11,24,25]. Worsening kinetics in the battery will typically broaden the peaks [16,18,22] and increase polarization. This is what is observed when the temperature is decreased or the charging rate is increased for P1

and P2. P1 flattens progressively with temperature at C/5 while vanishing completely at higher rates, with only a shoulder where the peak was previously located. P3, however, behaved in the opposite way to the other two peaks. At low rates, Figure 1a, the peak is located at 3.85 V with a considerably lower intensity than the other two peaks. At C/5, Figure 1b, the peak is no longer detectable, with a shoulder at lower voltages growing between 3.75 V and 3.85 V as temperature decreases instead. This trend continued at C/2, and the shoulder became a peak located between 3.75 and 3.80 V, the intensity of which overtook the former main peak P2 and maxed at 120 Ah/V, twice that observed at C/25. Finally, at 0.87C, P3 is still the most intense peak and all peaks followed the same trends, with some broadening and moving towards higher voltages as the temperature decreased.

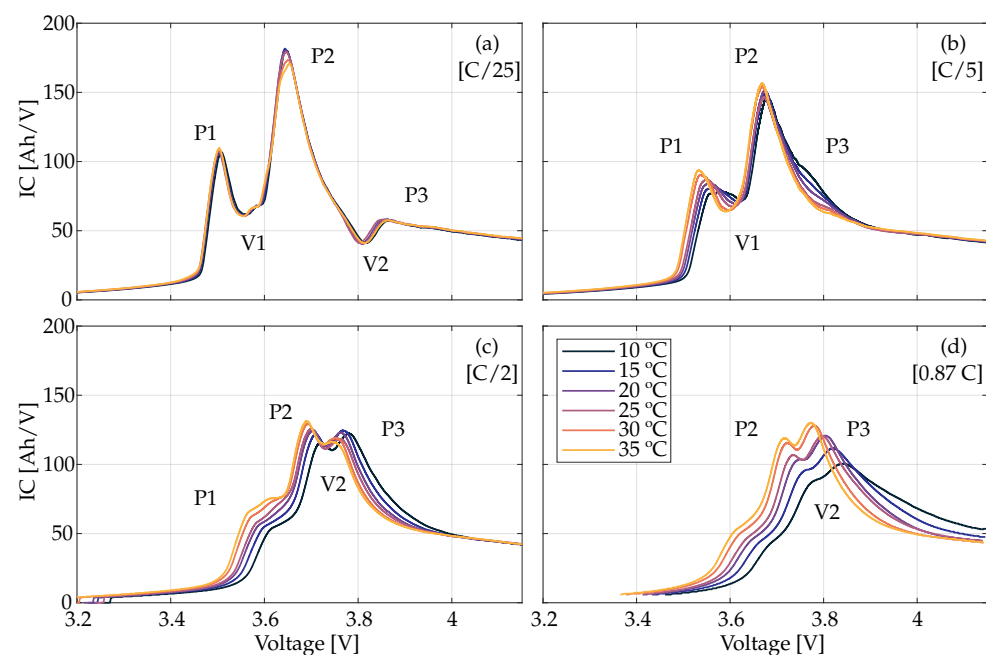


**Figure 1.** Full-cell IC curves attained at the BOL under various charging rates and temperatures; (a) C/25, (b) C/5, (c) C/2, (d) 0.87C [21].

### 3.1.2. From Half Cell to Full Cell

The half-cell data were used to emulate the full cell to associate the peaks and valleys observed in the full cell with the corresponding electrochemical reactions in both electrodes. Figure 2 shows the PE, NE, and full cell matching with the associated half-cell data with (a) the IC, (b) the voltage versus capacity, and (c) the DV signatures. The blue curves correspond to the NE, the red curves to the PE, and the pink ones to the full cell. The curves in solid pink correspond to the experimental full cell, while the curves in dotted pink were calculated from the matching of the NE and the PE (see next section).

Although both DV and IC curves display the same data, they allow for a different visualization of different aspects of cell performance. For the IC, and for each individual electrode, the plateaus of the voltage curve that correspond to phase transitions are transformed into peaks and their areas represent the associated capacity. The peak position is also influenced by polarization. At the full-cell level, the responses of the PE and NE are convoluted, which makes them complex to interpret. On the contrary, for DV curves, the full cell is the direct sum of the PE and NE response, making it easier to understand. However, the DV is insensitive to polarization and the peaks represent single phase regions while the valleys are associated with phase transitions. Peak and valley widths represent their relative capacity. More details on the comparison of both techniques can be found in [25] and in [26]. The PE voltage response in Figure 2b displays a large plateau and therefore a main peak at 3.75 V in the IC curve after derivation, indicating a phase transformation [24,27]. The broad peak observed at higher voltages corresponds to a solid

solution. This was expected, as high-voltage phase transitions are indiscernible in Ni-poor NMC materials such as the NMC532 used in this work, resulting in a single broad peak that represents the entire process [28]. In contrast, NMC materials with a higher Ni content, such as NMC811, may exhibit multiple peaks [24,29] in this region. The NE voltage response displays three well-marked plateaus in the voltage curve and thus three main peaks in the IC curve. In addition, the IC curve allows us to identify two additional smaller peaks. All correspond to the transition between the different stages of intercalation/de-intercalation of Li<sup>+</sup> into graphite [30].

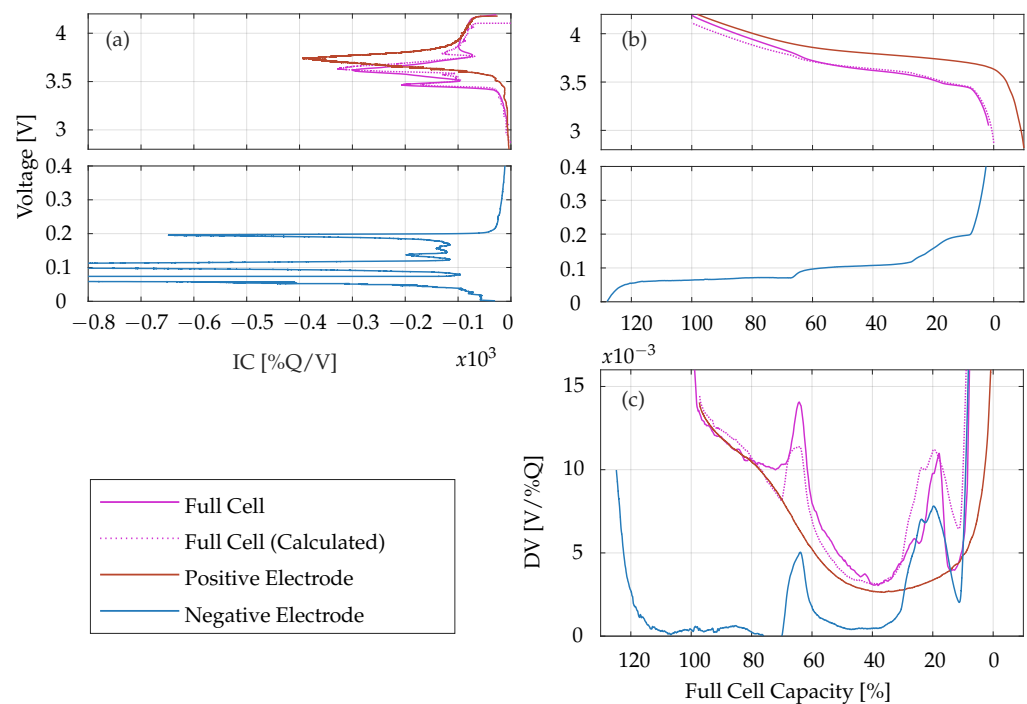


**Figure 2.** Voltage curves (b) derived from the analyzed electrodes and the respective IC (a) and DV (c) plots. The negative electrode (graphite) represented in blue, the positive electrode (NMC) in red, and the full cell shown in pink (solid pink refers to the fresh full cell and dotted pink represents the curve calculated from the positive and negative electrodes) [21].

From the peak indexation in the half cell, it can be deciphered that peak P1 corresponds to graphite stage 5, occurring during the beginning of the NMC phase transformation while charging. V1 corresponds to the two small graphitic transformations through the NMC phase transformation. P2 concurs with the remaining NMC phase transformations taking place during graphite stage 2. V2 corresponds to the LiC<sub>12</sub> single-phase region in between the two large graphitic plateaus. Finally, P3 corresponds to part of graphite stage 1 in either the NMC solid solution or phase transformation depending on the cell temperature, charging rate, or aging [25].

Although Figure 2 shows the relationship between the full cell, the PE, and the NE, it does not display the impact of changes in kinetics. The mechanistic models selected for this work allowed us to emulate the behavior of a cell under different conditions of charging rate or temperature by adjusting parameters such as the Ohmic Resistance Increase (ORI) or the Rate Degradation Factor (RDF) to mimic the kinetic changes [18]. To study the movement of the FOIs with worsening kinetics, a cell with a similar configuration of a graphite anode and an NMC532 cathode was emulated and the RDF was gradually increased to simulate worsening kinetics by up to 28-fold (i.e., the C/25 charge was degraded to a 0.9C charge). The ORI was tuned so that the overall polarization was kept constant [18]. Figure 3a shows the IC curves obtained through this procedure. As expected, flattening and broadening of the peaks were observed as the RDF increased. Despite the overall ORI adjustment, V2 shifted to the left until it reached the same voltage as P2, which produces the double



peak also observed in Figure 1. This effect can also be observed in the evolution of the DV curve in Figure 3b. When the C-rate is increased, the second peak, corresponding to V2, shifted towards lower SOC levels, from the initial 67% to less than 20%, crossing the region where P2 is located. This explains the counter-intuitive P3 peak movement and verifies that graphite stage 1 can occur not only during the NMC solid solution, but also during the phase transformation, inducing a new sharp peak with different behavior to the other peaks, as previously proposed [25].

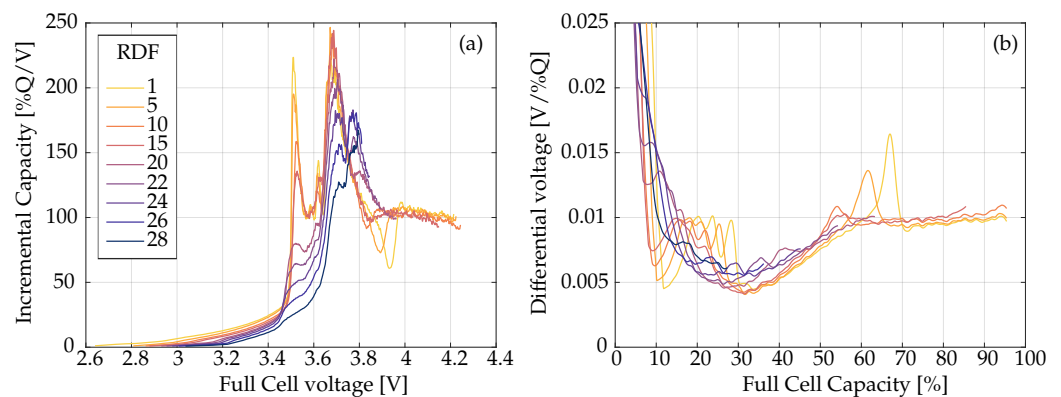


**Figure 3.** IC (a) and DV (b) curves emulating different C-rates.

### 3.2. Peak Tracking and SOH Estimation

#### 3.2.1. Calendar Aging Results

Figure 4a shows the capacity progression during the calendar aging test, revealing a gradual capacity decrease as the temperature rises. The cell stored at 25 °C and 90% SOC showed a 10% capacity loss compared to the initial capacity. When the temperature increased to 35 °C, the capacity fade increased by 50%, and it reached 150% when the temperature was increased to 45 °C. The effect of an increased temperature on cells stored at 50% SOC also contributed to the capacity degradation, but it was significantly lower. By the conclusion of the experiments, the cell aged at 35 °C had a 12% capacity fade, while the cell stored at 45 °C had a 15% capacity drop. This implies that when the temperature increases from 35 °C to 45 °C, at 50% SOC there is a 25% increase in capacity loss, whereas at 90% SOC, the same temperature led to a 65% increase in capacity loss. Figure 4b provides a summarized representation, enhancing the understanding of the influence of temperature and SOC on capacity loss over a 12-month period.

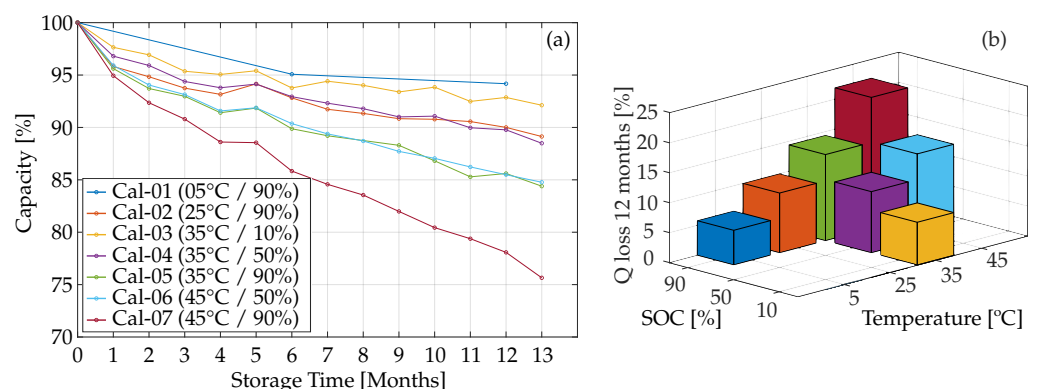


**Figure 4.** Capacity fade of the tested cells under calendar aging conditions (a) and capacity loss after 12 months of testing (b).

#### 3.2.2. Incremental Capacity Signature Evolution

Since the objective of this work is to be able to relate the SOH to the movement of the different FOIs, Figure 5 presents an example of how IC signatures changed with aging for



the cell stored at 45 °C and 90% SOC for the nine combinations of current and temperature applied during the RPT. This particular experiment was chosen due to its higher capacity loss, but the rest of the cells were verified to display a similar overall IC evolution upon aging, as shown in Figure 6, where it can be seen that the evolution of the IC curves is consistent between the experiments. The different extents of the decreasing intensities and shifts towards higher voltages for P1 and P2 indicate different amounts of loss of lithium inventory, without any significant loss of active material for the PE or the NE [25]. Figure 5 shows that for the RPT curves measured at 10 °C (first column), the high polarization, together with an incomplete discharge, prevents P1 from being observed because the previous discharge was incomplete. At C/5 (first row), P2 and P3 can be clearly observed during the first stages of the battery life, but their intensity decreases with aging. At C/2 (second row), two similar peaks are observed, but P3 is this time the predominant peak during the initial months of testing. At 0.87C (third row), the curve is so broad that only one peak can be observed at the location of P3.

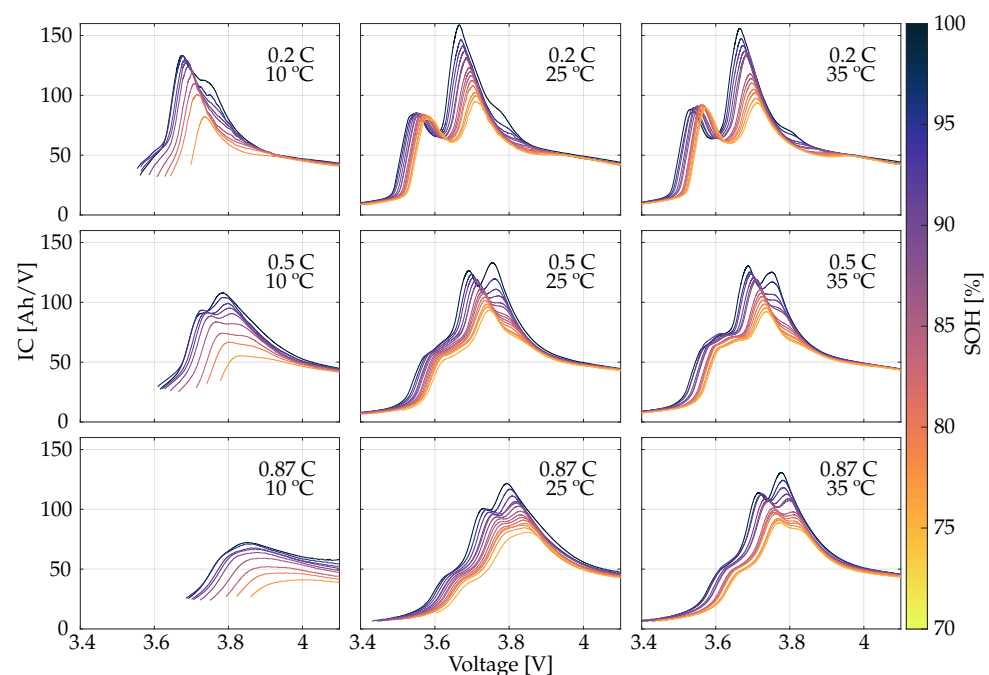


**Figure 5.** Evolution of the IC curve for the full cell under varying conditions of temperature and C-rate for cell cal-07 [21].

At 25 °C and 35 °C, it is possible to observe P1, and the peak shape was the most defined at C/5. Its intensity remained constant with aging, with only a slight shift towards higher voltages because of the loss of lithium inventory and the increase in internal resistance. P2 remained the main feature under these conditions, although its shape and size nearly matched P1 at the completion of the aging test. P3 was almost imperceptible at C/5, where it was only noticeable at the BOL as a localized shoulder at 3.8 V. However, with an increasing charging rate, it became more visible and equalled or surpassed P2 in intensity. Its intensity, however, decreased at a faster rate than P2 with aging. At 0.87C, as the cell degraded, P3 and P2 gradually formed a single peak. In general, it is observed that when the current increases or the temperature decreases, P1 and P2 flattened and shifted to greater voltages, even vanishing at certain conditions, while P3 remained practically at the same voltage at C/5 and 0.87C and became more prominent as the charging rate increased. Further results can be found in [21].

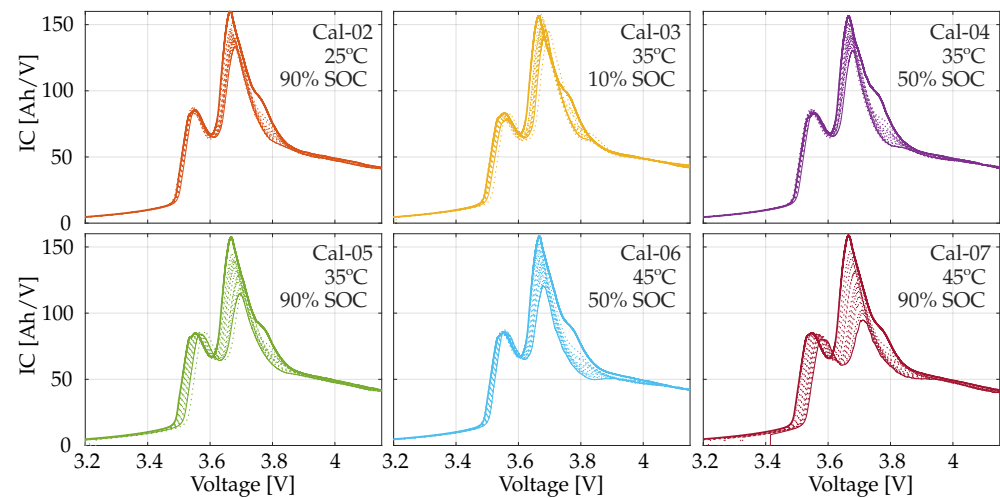


**Figure 6.** IC evolution of six different cells measured at 25 °C and 0.2C.

### 3.2.3. SOH Estimation

All the FOIs were investigated and their performance for SOH estimation is summarized in Table 2. In this work, the SOH was defined as the charging capacity relative to the capacity at the BOL, both measured at 25 °C and C/5 as shown in Equation (1). The FOIs were compared using  $R^2$ , the Mean Absolute Error (MAE), and the Root Mean Square Error (RMSE).  $R^2$  indicates the percentage of the SOH that can be explained by the feature in question; the closer it is to 1, the better this relationship is. Both the MAE and RMSE indicate the average prediction error in the same units as the variable of interest (SOH (%)). The RMSE is always equal to or higher than the MAE because it gives a higher weight to large errors, so divergent values may indicate the presence of unwanted large errors. Error values under 0.7 for  $R^2$  are not shown, as it is understood that below this value, the model does not show a good correlation. The values marked with “X” indicate that the feature is not visible or detectable under those conditions. Values in bold represent the best FOI for SOH estimation under the specified test conditions.

$$SOH = \frac{Q_{RPT}}{Q_{BOL}} \times 100; \quad Q[C/5 \ \& \ 25 \ ^\circ C] \quad (1)$$

Figure 7 showcases selected examples from Table 2. Figure 7a,b presents the evolution of the intensity and position of P2 versus SOH using a charging rate of C/5. At 25 °C and 35 °C, both P2-related FOIs showed a mostly linear behavior with the SOH, with the peak intensity being the best ( $R^2 > 0.9$  versus  $\approx 0.75$ ). At 10 °C, the intensity evolution shows a slightly non-linear behavior at the beginning of the cell life; after 90% SOH, the behavior becomes similar to that of the tests at 25 and 35 °C. Looking at a higher rate, C/2, Figure 7c,d shows the evolution of the position of P2 FOIs versus the SOH. At this current, P2 is no longer a valid indicator at low temperatures, whereas a similar behavior is observed at 25 °C and 35 °C to the IC intensity variations best explaining SOH variations. The relationship between the intensity of P3 and SOH is shown in Figure 7e,f. When charging currents of C/2 are used, the estimation accuracy at low temperatures decays, while at 0.87C, the feature can no longer be used to estimate the battery charging capacity correctly. Overall, the correlation for P3 vs. SOH is similar to that of P2; however, P3 is no longer visible between 80 and 90% of the SOH for the cases analyzed, while P2 is present until the end of the aging tests ( $\approx 75\%$  SOH).

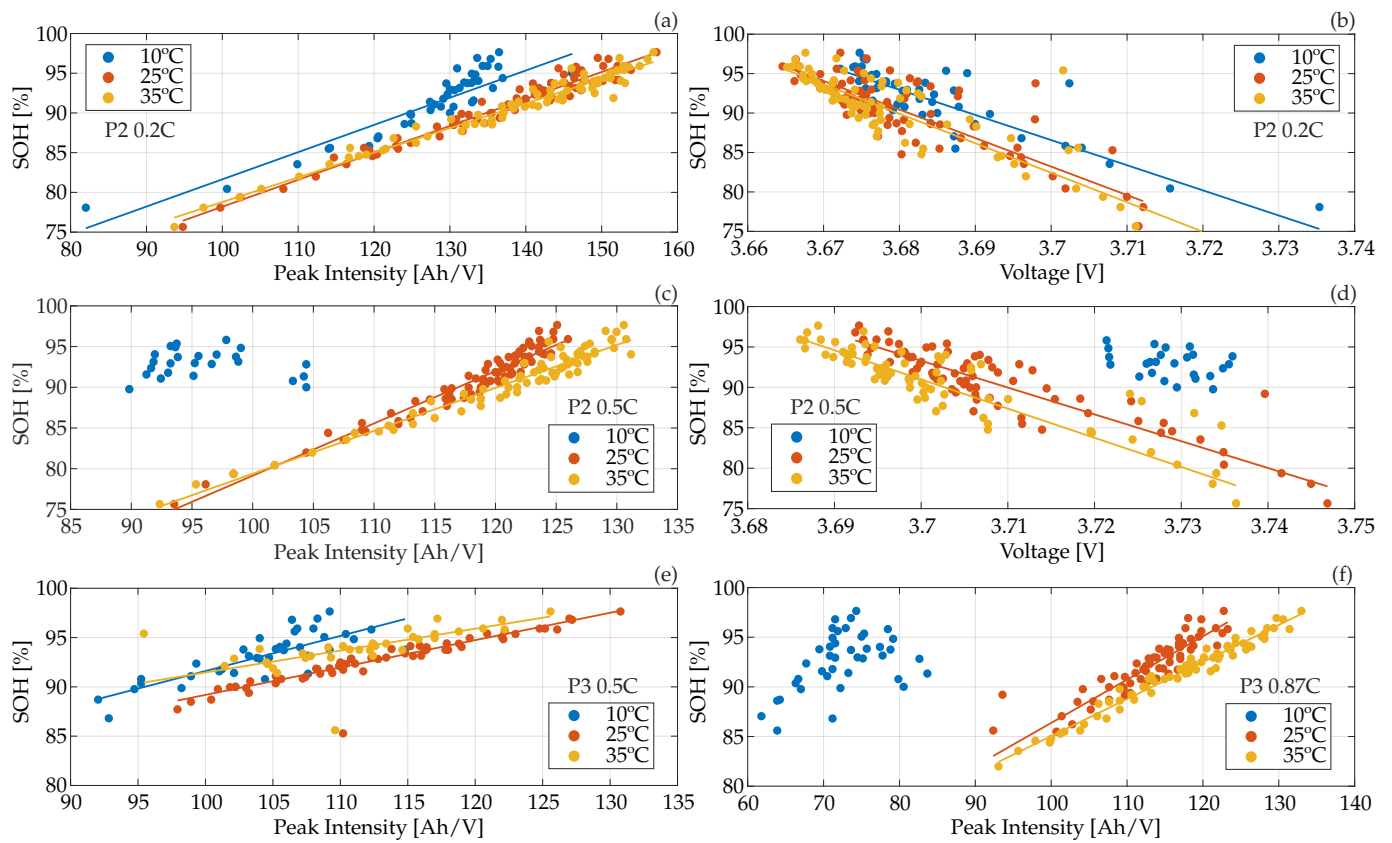


**Figure 7.** Correlation between SOH and feature intensity or voltage. (a,b) P2/0.2C; (c,d) P2/0.5C; (e) P3/0.5C; (f) P3/0.87C.

**Table 2.** Statistical metrics of the analyzed FOIs under various temperature and current conditions. Best performance in bold [21].

			10 °C			25 °C			35 °C		
			R <sup>2</sup>	MAE	RMSE	R <sup>2</sup>	MAE	RMSE	R <sup>2</sup>	MAE	RMSE
Intensity	P2	C/5	0.79	1.56	2.01	<b>0.95</b>	<b>0.71</b>	<b>0.98</b>	<b>0.97</b>	<b>0.65</b>	<b>0.84</b>
		C/2	0.02	-	-	0.94	0.86	1.12	<b>0.94</b>	<b>0.83</b>	<b>1.08</b>
		0.87C	X	X	X	0.43	-	-	0.9	1.13	1.49
	P3	C/5	X	X	X	X	X	X	X	X	X
		C/2	0.6	-	-	<b>0.95</b>	<b>0.44</b>	<b>0.49</b>	0.76	0.81	0.83
		0.87C	0.18	-	-	<b>0.86</b>	<b>0.95</b>	<b>1.17</b>	<b>0.97</b>	<b>0.49</b>	<b>0.64</b>
	V2	C/5	X	X	X	X	X	X	X	X	X
		C/2	0.25	-	-	0.79	0.83	1.06	0.76	0.95	1.03
		0.87C	0.73	0.8	1.09	0.69	-	-	0.85	1.37	1.54
Voltage	P2	C/5	0.79	1.61	2.03	0.73	1.93	2.48	0.8	2.09	2.41
		C/2	0.1	-	-	0.84	1.53	1.92	0.86	1.68	1.95
		0.87C	X	X	X	0.54	-	-	0.78	1.7	2.23
	P3	C/5	X	X	X	X	X	X	X	X	X
		C/2	0.7	1.66	1.82	0.03	-	-	0.02	-	-
		0.87C	0.62	-	-	0.35	-	-	0.58	-	-
	V2	C/5	X	X	X	X	X	X	X	X	X
		C/2	0.78	1.24	1.38	0.73	1.26	1.45	0.83	1.43	1.24
		0.87C	0.47	-	-	0.77	2.36	2.5	0.64	-	-

Overall, the intensity of the FOIs correlated better than their voltage. It is observed that the intensity of P2 would be a consistent indicator at temperatures above 25 °C for currents below C/2. As the current increases, P3 would then replace it as the best feature to estimate the SOH. Both indicators show similar metrics, without significant differences between them, and with a reduced RMSE of around 1%. However, P2 is present in a larger SOH range than P3, so it would be the logical choice, unless the test is required to be performed at high currents, in which case P3 would be better. V2 does not enable accurate SOH estimation unless under low temperature conditions, where it could be a good alternative.

When the above models are used with data at different temperatures and/or charging currents, the great importance of these parameters in the estimation of the SOH can be inferred. Table 3 shows the error obtained when trying to estimate the SOH under different conditions to those of the model; for example, in the case of using the P2 intensity at 25 °C and C/5 for estimating the SOH of a vehicle at 15 °C, the RMSE would increase from 0.98 to 3.99. Similarly, if the estimator used is P2 intensity at 25 °C and C/2, an analysis of the battery using C/5 would increase the RMSE from 1.12 to 12.71.

**Table 3.** RMSE obtained for conditions different from those under which the model has been trained for the feature intensity P2.

			Model					
			10 °C		25 °C		35 °C	
			C/5	C/2	C/5	C/2	C/5	C/2
Actual conditions	10 °C	C/5	<b>2.01</b>	-	3.99	7.31	4.23	4.21
		C/2	12.71	-	16.24	16.77	15.48	15.99
	25 °C	C/5	3.66	-	<b>0.98</b>	12.71	1.09	8.54
		C/2	3.53	-	6.75	<b>1.12</b>	6.73	2.21
	35 °C	C/5	4.18	-	1.11	14.01	<b>0.84</b>	9.59
		C/2	2.53	-	5.54	2.6	5.63	<b>1.08</b>

In general, it is observed that, under the tested conditions, high currents can be used to accurately estimate the SOH of a battery. However, it is important to note that for different driving conditions, more experiments would have to be conducted to validate the performance of the estimation model. A clear limitation is also observed at low temperatures, where not only is the number of available indicators reduced, but also the performance of the estimation model. Therefore, further studies are required to assess the accuracy of the SOH estimation model under different conditions.

#### 4. Conclusions

This work presents a comprehensive analysis of the performance and accuracy of different incremental capacity features and their behavior at different temperatures for the estimation of the state of health.

The results show that the use of different features allows us to obtain reliable estimation results, even at high charging rates of up to 0.87C. We believe this could be a significant advantage, particularly in the case of deployed vehicles, as it would considerably reduce testing times. Furthermore, this method enables the possibility of conducting tests at uncontrolled or variable temperatures during charging.

A correct identification of FOIs is crucial in order to obtain accurate SOH estimations under variable current and temperature conditions. Although our results have not determined an exclusive FOI suitable for all the situations analyzed, different reliable indicators have been identified that allow for accurate estimations under a wide range of conditions. The RMSE obtained for temperatures of 25 °C and 35 °C is around 1%, and it is 2% for

10 °C, where the estimation becomes complex due to the strong deformation suffered by the IC curve, especially at high currents.

**Author Contributions:** Conceptualization, A.G., M.D., D.-I.S. and E.S.; methodology, A.G., M.D., J.G. and D.-I.S.; software, A.G., M.D. and E.S.; validation, A.G.; formal analysis, A.G.; investigation, A.G., J.G. and D.-I.S.; resources, M.D., D.-I.S. and E.S.; data curation, A.G. and M.D.; writing—original draft preparation, A.G.; writing—review and editing, M.D., J.G., D.-I.S. and E.S.; visualization, A.G.; supervision, M.D., D.-I.S. and E.S.; project administration, D.-I.S. and E.S.; funding acquisition, D.-I.S. and E.S. All authors have read and agreed to the published version of the manuscript.

**Funding:** This work was part of the Workshop Automated Battery Tester (WABAT) project, project no. 64019-0056. The authors gratefully acknowledge EUDP Denmark for providing the financial support necessary for carrying out this work.

**Data Availability Statement:** The data are not publicly available due to privacy policy.

**Conflicts of Interest:** The authors declare no conflict of interest.

## References

1. Lockheed Idaho Technologies Co. *USABC Electric Vehicle Battery Test Procedures Manual. Revision 2*; USDOE: Washington, DC, USA, 1996. [CrossRef]
2. Dubarry, M.; Baure, G.; Devie, A. Durability and Reliability of EV Batteries under Electric Utility Grid Operations: Path Dependence of Battery Degradation. *J. Electrochem. Soc.* **2018**, *165*, A773–A783. [CrossRef]
3. Gering, K.L.; Sazhin, S.V.; Jamison, D.K.; Michelbacher, C.J.; Liaw, B.Y.; Dubarry, M.; Cugnet, M. Investigation of path dependence in commercial lithium-ion cells chosen for plug-in hybrid vehicle duty cycle protocols. *J. Power Sources* **2011**, *196*, 3395–3403. [CrossRef]
4. Raj, T.; Wang, A.; Monroe, C.; Howey, D. Investigation of Path Dependent Degradation in Lithium-Ion Batteries. *Batter. Supercaps* **2020**, *3*, 1377–1385. [CrossRef]
5. Knap, V.; Stroe, D.I.; Purkayastha, R.; Walus, S.; Auger, D.J.; Fotouhi, A.; Propp, K. Reference Performance Test Methodology for Degradation Assessment of Lithium-Sulfur Batteries. *J. Electrochem. Soc.* **2018**, *165*, 1601–1609. [CrossRef]
6. Chen, L.; Lü, Z.; Lin, W.; Li, J.; Pan, H. A new state-of-health estimation method for lithium-ion batteries through the intrinsic relationship between ohmic internal resistance and capacity. *Meas. J. Int. Meas. Confed.* **2018**, *116*, 586–595. [CrossRef]
7. Dubarry, M.; Berecibar, M.; Devie, A.; Anseán, D.; Omar, N.; Villarreal, I. State of health battery estimator enabling degradation diagnosis: Model and algorithm description. *J. Power Sources* **2017**, *360*, 59–69. [CrossRef]
8. Schaltz, E.; Stroe, D.I.; Norregaard, K.; Ingvarlsen, L.S.; Christensen, A. Incremental Capacity Analysis Applied on Electric Vehicles for Battery State-of-Health Estimation. *IEEE Trans. Ind. Appl.* **2021**, *57*, 1810–1817. [CrossRef]
9. Berecibar, M.; Devriendt, F.; Dubarry, M.; Villarreal, I.; Omar, N.; Verbeke, W.; Mierlo, J.V. Online state of health estimation on NMC cells based on predictive analytics. *J. Power Sources* **2016**, *320*, 239–250. [CrossRef]
10. Zhang, Y.; Liu, Y.; Wang, J.; Zhang, T. State-of-health estimation for lithium-ion batteries by combining model-based incremental capacity analysis with support vector regression. *Energy* **2022**, *239*, 121986. [CrossRef]
11. Li, Y.; Abdel-Monem, M.; Gopalakrishnan, R.; Berecibar, M.; Nanini-Maury, E.; Omar, N.; van den Bossche, P.; Mierlo, J.V. A quick on-line state of health estimation method for Li-ion battery with incremental capacity curves processed by Gaussian filter. *J. Power Sources* **2018**, *373*, 40–53. [CrossRef]
12. Jiang, B.; Dai, H.; Wei, X. Incremental capacity analysis based adaptive capacity estimation for lithium-ion battery considering charging condition. *Appl. Energy* **2020**, *269*, 115074. [CrossRef]
13. Li, X.; Yuan, C.; Wang, Z. State of health estimation for Li-ion battery via partial incremental capacity analysis based on support vector regression. *Energy* **2020**, *203*, 117852. [CrossRef]
14. Dubarry, M.; Beck, D. Analysis of Synthetic Voltage vs. Capacity Datasets for Big Data Li-ion Diagnosis and Prognosis. *Energies* **2021**, *14*, 2371. [CrossRef]
15. Lin, Y.; Jiang, B.; Dai, H. Battery Capacity Estimation Based on Incremental Capacity Analysis Considering Charging Current Rate. *World Electr. Veh. J.* **2021**, *12*, 224. [CrossRef]
16. Chen, Y.; Torres-Castro, L.; Chen, K.H.; Penley, D.; Lamb, J.; Karulkar, M.; Dasgupta, N.P. Operando detection of Li plating during fast charging of Li-ion batteries using incremental capacity analysis. *J. Power Sources* **2022**, *539*, 231601. [CrossRef]
17. Maures, M.; Mathieu, R.; Capitaine, A.; Delétage, J.Y.; Vinassa, J.M.; Briat, O. An Incremental Capacity Parametric Model Based on Logistic Equations for Battery State Estimation and Monitoring. *Batteries* **2022**, *8*, 39. [CrossRef]
18. Schindler, S.; Baure, G.; Danzer, M.A.; Dubarry, M. Kinetics accommodation in Li-ion mechanistic modeling. *J. Power Sources* **2019**, *440*, 227117. [CrossRef]
19. MarkLines Co., Ltd. Nissan LEAF Teardown: Lithium-Ion Battery Pack Structure. 2018. Available online: [https://www.marklines.com/en/report\\_all/rep1786\\_201811](https://www.marklines.com/en/report_all/rep1786_201811) (accessed on 17 June 2022).

20. Dubarry, M.; Qin, N.; Brooker, P. Calendar aging of commercial Li-ion cells of different chemistries—A review. *Curr. Opin. Electrochem.* **2018**, *9*, 106–113. [[CrossRef](#)]
21. Gismero, A. Electric Vehicle Batteries State Estimation under a Wide Range of Test and Aging Conditions. Ph.D. Thesis, Aalborg Universitetsforlag, Aalborg, Denmark, 2022. [[CrossRef](#)]
22. Dubarry, M.; Truchot, C.; Liaw, B.Y. Synthesize battery degradation modes via a diagnostic and prognostic model. *J. Power Sources* **2012**, *219*, 204–216. [[CrossRef](#)]
23. Dubarry, M. 'Alawa: A Unique Mechanistic Model for Battery Diagnosis and Prognosis. Available online: <https://www.soest.hawaii.edu/HNEI/alawa> (accessed on 3 October 2022).
24. Jung, R.; Metzger, M.; Maglia, F.; Stinner, C.; Gasteiger, H. Oxygen Release and Its Effect on the Cycling Stability of  $\text{LiNi}_x\text{Mn}_y\text{Co}_z\text{O}_2$  (NMC) Cathode Materials for Li-Ion Batteries. *J. Electrochem. Soc.* **2017**, *164*, A1361–A1377. [[CrossRef](#)]
25. Dubarry, M.; Anseán, D. Best practices for incremental capacity analysis. *Front. Energy Res.* **2022**, *10*, 1023555. [[CrossRef](#)]
26. Barai, A.; Uddin, K.; Dubarry, M.; Somerville, L.; McGordon, A.; Jennings, P.; Bloom, I. A comparison of methodologies for the non-invasive characterisation of commercial Li-ion cells. *Prog. Energy Combust. Sci.* **2019**, *72*, 1–31. [[CrossRef](#)]
27. Hudson, B.G.; Mason, S.E. Metal Release Mechanism and Electrochemical Properties of  $\text{Li}_x(\text{Ni}_{1/3}\text{Mn}_{1/3}\text{Co}_{1/3})\text{O}_2$ . *Appl. Sci.* **2022**, *12*, 4065. [[CrossRef](#)]
28. Xu, C.; Reeves, P.J.; Jacquet, Q.; Grey, C.P. Phase Behavior during Electrochemical Cycling of Ni-Rich Cathode Materials for Li-Ion Batteries. *Adv. Energy Mater.* **2021**, *11*, 2003404. [[CrossRef](#)]
29. Anseán, D.; Baure, G.; González, M.; Cameán, I.; García, A.B.; Dubarry, M. Mechanistic investigation of silicon-graphite/ $\text{LiNi}_{0.8}\text{Mn}_{0.1}\text{CO}_{0.1}\text{O}_2$  commercial cells for non-intrusive diagnosis and prognosis. *J. Power Sources* **2020**, *459*, 227882. [[CrossRef](#)]
30. Dahn, J.R. Phase diagram of  $\text{Li}_x\text{C}_6$ . *Phys. Rev. B* **1991**, *44*, 9170–9177. [[CrossRef](#)]

**Disclaimer/Publisher's Note:** The statements, opinions and data contained in all publications are solely those of the individual author(s) and contributor(s) and not of MDPI and/or the editor(s). MDPI and/or the editor(s) disclaim responsibility for any injury to people or property resulting from any ideas, methods, instructions or products referred to in the content.